Electronic Supplementary Material (ESI) for Journal of Materials Chemistry A.
This journal is © The Royal Society of Chemistry 2018

Supporting Information

Ultrafine Cable-like WC/W_2C Heterojunction Nanowires Covered by Graphitic Carbon towards High Efficient Electrocatalytic Hydrogen Evolution

Lu-Nan Zhang,[a] Yuan-Yuan Ma,[a] Zhong-Ling Lang,[a*] Yong-Hui Wang,[a] Shifa Ullah Khan,[a] Gang Yan,[a] Hua-Qiao Tan,[a*] Hong-Ying Zang,[a] Yang-guang Li[a*]

[a] *Key Laboratory of Polyoxometalate Science of Ministry of Eduction, Faculty of Chemistry, Northeast Normal University, Changchun, 130024 (P.R. China)*

[*]Corresponding authors

E-mail adress: langzl554@nenu.edu.cn (Z.L. Lang), tanhq870@nenu.edu.cn. (H.Q. Tan), liyg658@nenu.edu.cn. (Y.G. Li).

Postal address: Northeast Normal University, Renmin Street No. 5268, Changchun, Jilin Province, 130024, P. R. China

Table of contents

Experimental Section

Preparation of the working electrodes

The working electrode was prepared as follows: 2 mg of catalyst was dispersed in 500 μl of 0.5 wt% Nafion solution. After ultrasonication for 1 h, 6 μl of the homogeneous ink was dropped on the surface of a glassy carbon electrode (GCE) with a diameter of 3 mm. The loading of catalyst is about 0.34 mg cm^{-2}. The electrode was then dried in air.

Preparation of electrolytes

0.5 M H_2SO_4 (pH=0.30), 0.05 M H_2SO_4 + 0.45 M Na_2SO_4 (pH=1.54), 5 mM H_2SO_4 + 0.49 M Na_2SO_4 (pH=2.73), 0.5 mM H_2SO_4 + 0.49 M Na_2SO_4 (pH=3.65), 0.05 mM H_2SO_4 + 0.49 M Na_2SO_4 (pH=4.63), 5 μM H_2SO_4 + 0.49 M Na_2SO_4 (pH=5.65), 0.5 μM H_2SO_4 +0.49 M Na_2SO_4 (pH=5.80), 1 M KOH (pH=14.00), 0.1 M KOH + 0.6 M K_2SO_4 (pH=12.80), 0.01 M KOH + 0.66 M K_2SO_4 (pH=12.02), 1 mM KOH + 0.66 M K_2SO_4 (pH=11.33), 0.1 mM KOH + 0.66 M K_2SO_4 (pH=9.46), 0.01 mM KOH + 0.66 M K_2SO_4 (pH=9.33), 1 μM KOH + 0.66 M K_2SO_4 (pH=8.19).

1 M PBS was prepared by dissolving 1.361 g KH_2PO_4 in 10 mL deionized water, and the pH of the mixture was adjusted to 7.00 with 1 M KOH.

Physical characterization

The electron transmission microscopy (TEM) was performed on a JEOL-2100F transmission electron microscope. The powder X-ray diffraction (PXRD) measurements were carried out on a Rigaku D/max-IIB X-ray diffractometer with Cu-Kα radiation (λ=1.5418Å). Raman spectrum was recorded on a Raman

spectrometer (JY, Labram HR 800). The X-ray photoelectron spectroscopy (XPS) measurements were performed on an ESCALAB 250 spectrometer (Thermo Electron Corp.) with Al Kα radiation (hυ=1486.6 eV) as the excitation source. The interrelated energy dispersive X-ray detector (EDX) spectra were achieved by using a SU8000 ESEM FEG microscope. The nitrogen sorption measurement was obtained on an ASAP 2020 (Micromeritics, USA).

Electrochemical measurements

All the cyclic voltammetry (CV) and linear sweep voltammetry (LSV) measurements were performed with a typical three-electrode system using a CHI660E electrochemical workstation (CH Instruments, China) at 25 ^{o}C. A modified glassy carbon electrode (GCE, d=3 mm) was served as the working electrode. A carbon rod was used as the counter electrode, and a saturated calomel electrode (SCE) as the reference electrode. For comparison, the bare glassy carbon electrode (GCE) and commercial Pt/C catalyst (20 wt% Pt/XC-72R) are also evaluated as reference samples. In all measurements, the potential measured against an SCE electrode were calibrated to the potentials referenced to the reversible hydrogen electrode (RHE), according to $E_{RHE}=E_{SCE}+E^{\ominus}_{SCE}+0.059$ pH. All the electrolytes were N_2 saturated before the measurements. The linear sweep voltammetry (LSV) measurements were carried out with a scan rate of 5mv s^{-1}. Tafel slopes were determined by fitting the linear regions of Tafel plots according to the Tafel equation ($\eta=b \log j + a$). Electrochemical stability was measured using cyclic voltammetric sweeps at 100 mV s^{-1} between - 0.2 V and - 0.4 V (*vs.* SCE). To evaluate electrochemically active surface

area (ECSA), the scan rate of cyclic voltammograms was set to 25, 50, 75, 100, 125, 150, 175, and 200 mv s^{-1}. The range of voltage was from -0.1 to 0.1 V (*vs.* SCE, in 0.5 M H_2SO_4) and -1.1 to -0.9 V (*vs.* SCE, in 1 M KOH), respectively. The long-term (45 hrs) stability was also tested at controlled overpotential. Electrochemical impedance spectroscopy (EIS) was performed on a PARSTAT 2273 electrochemical configuration (Princeton Applied Research Instrumentation, USA) with frequency from 0.01 to 100000 Hz and an amplitude of 10 mV. The EIS spectra were fitted by the Z-SimpWin software. All the electrochemistry measurements are represented with IR compensation.

Theoretical Section

Computational methods

Theoretical modeling based on periodic density functional theory (DFT) method were carried out with *Vienna ab initio simulation package* (VASP 5.3 version) to evaluate the adsorption ability of H [S1-S4]. For the description of electron exchange-correlation, the Perdew−Burke-Ernzerhof (PBE) functional within the generalized-gradient approximation range was applied [S5]. The valence electrons were considered as following for per species, $5d^4 6s^2$ for W, $2s^2 sp^2$ for C, and $1s^1$ for H. The interaction between these valence electrons and the corresponding pseudopotential was described using the projector augmented wave (PAW) scheme [S6]. The kinetic energy cutoff was chosen to be 400 eV. Geometric optimizations for all models were performed until self-consistency, with thresholds of 1×10^{-5} eV and 0.03 eV/Å for electronic and ionic convergence, respectively. The K-point mesh for all models was set to be 3×3×1

with Monkhorst-Pack automatic grid [S7].

The Gibbs free energy for hydrogen adsorption was defined as:

$$\Delta G = \Delta E + \Delta E_{ZPE} - T\Delta S$$

Where ΔE is the adsorption energies of H on the surface ($\Delta E = E_{total} - E_{slab} - 1/2E_{H2}$), ΔE_{ZPE} is the zero-point energy difference between the adsorbed state of the system and the gas phase state for H by referring the equation of $\Delta E_{ZPE} = E_{ZPE(H^*)} - 1/2E_{ZPE(H2)}$. In the current case, the $E_{ZPE(H2)}$ is calculated to be 0.278 eV. Similarly, ΔS is the entropy difference between the adsorbed and gas phase H, it can be obtained from the equation $\Delta S = S(H^*) - 1/2\ S(H_2) \approx -1/2\ S(H_2)$, in which the vibrational entropy of H* was negligible. Since $TS(H_2)$ is known to be 0.41 eV for H_2 at 300 K and 1 atm, so the corresponding TΔS is obtained as –0.205 eV.

Computational models

Bulk WC and W_2C both were adopted the hexagonal structure, and the lattice parameters (*a* = *b* = 3.057 Å, *c* = 4.669 Å for W_2C, *a* = *b* = 2.918 Å, *c* = 2.845 Å for WC) were calculated in accordance with experimental values (*a* = *b* = 2.990 Å, *c* = 4.720 Å for W_2C, *a = b = 2.906 Å, c = 2.837* for WC). Supplementary Figure S15 shows the theoretical models of the studied systems. The clean WC (001) and W_2C (001) surfaces were composed of three layers of carbides with vacuum space larger than 15 Å. In both cases, the model surface consisted of a 4×4 supercell in which the bottom two layers were fixed while the top layer was allowed to relax. The lattice constants of WC and W_2C are 2.918 (*a*=*b*) and 3.057 Å, respectively; thus, there is almost lattice match with error of only 4%. The composite W_2C/WC surfaces, one

layer of WC (001) carbide (or W_2C carbide) was constructed onto three W_2C (001) (WC) layers. In order to simulate the models with nanowire character, suspended WC (a W_8C_8 cluster periodic in y direction) and W_2C (a $W_{24}C_{12}$ cluster periodic in y direction) nanowires that periodic in the y direction was constructed on the W_2C (001) and WC (001) surface respectively.

Supporting Figures

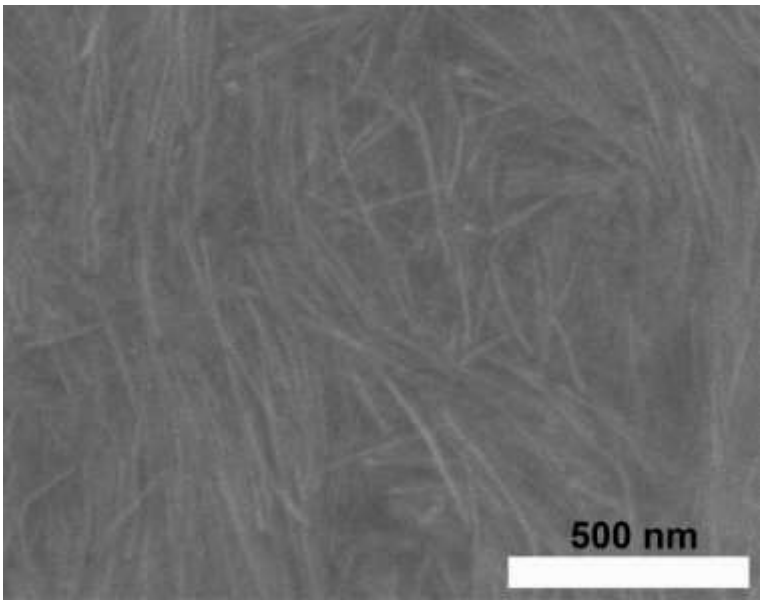

Fig. S1 SEM image of precursor $W_{18}O_{49}$ NWs.

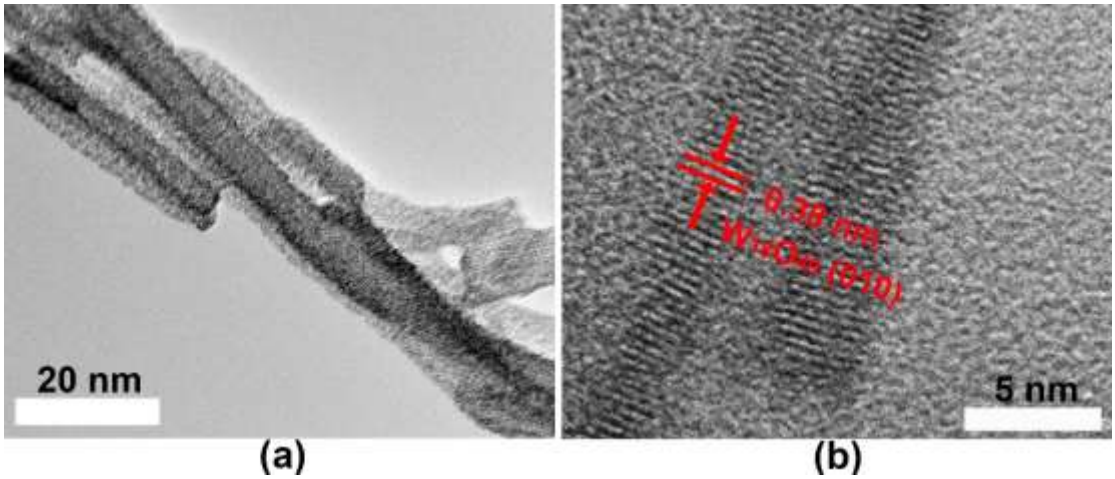

Fig. S2 (a) TEM and (b) HRTEM images of precursor $W_{18}O_{49}$ NWs.

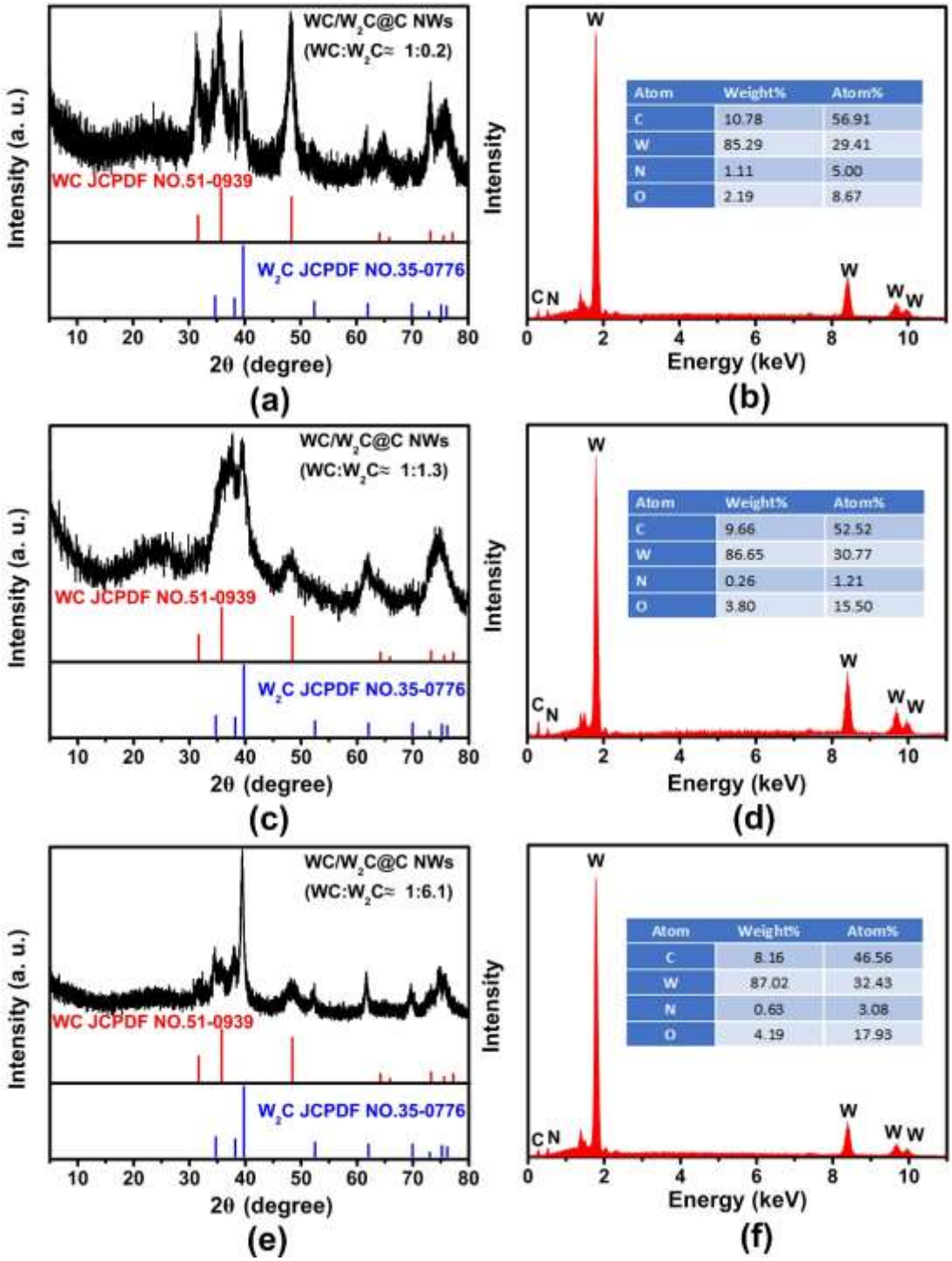

Fig. S3 (a)-(b) Powder XRD pattern and EDX spectrum of WC/W_2C@C NWs (WC:W_2C≈1:0.2); (c)-(d) Powder XRD pattern and EDX spectrum of WC/W_2C@C NWs (WC:W_2C≈1:1.3); (e)-(f) Powder XRD pattern and EDX spectrum of WC/W_2C@C NWs (WC:W_2C≈1:6.1).

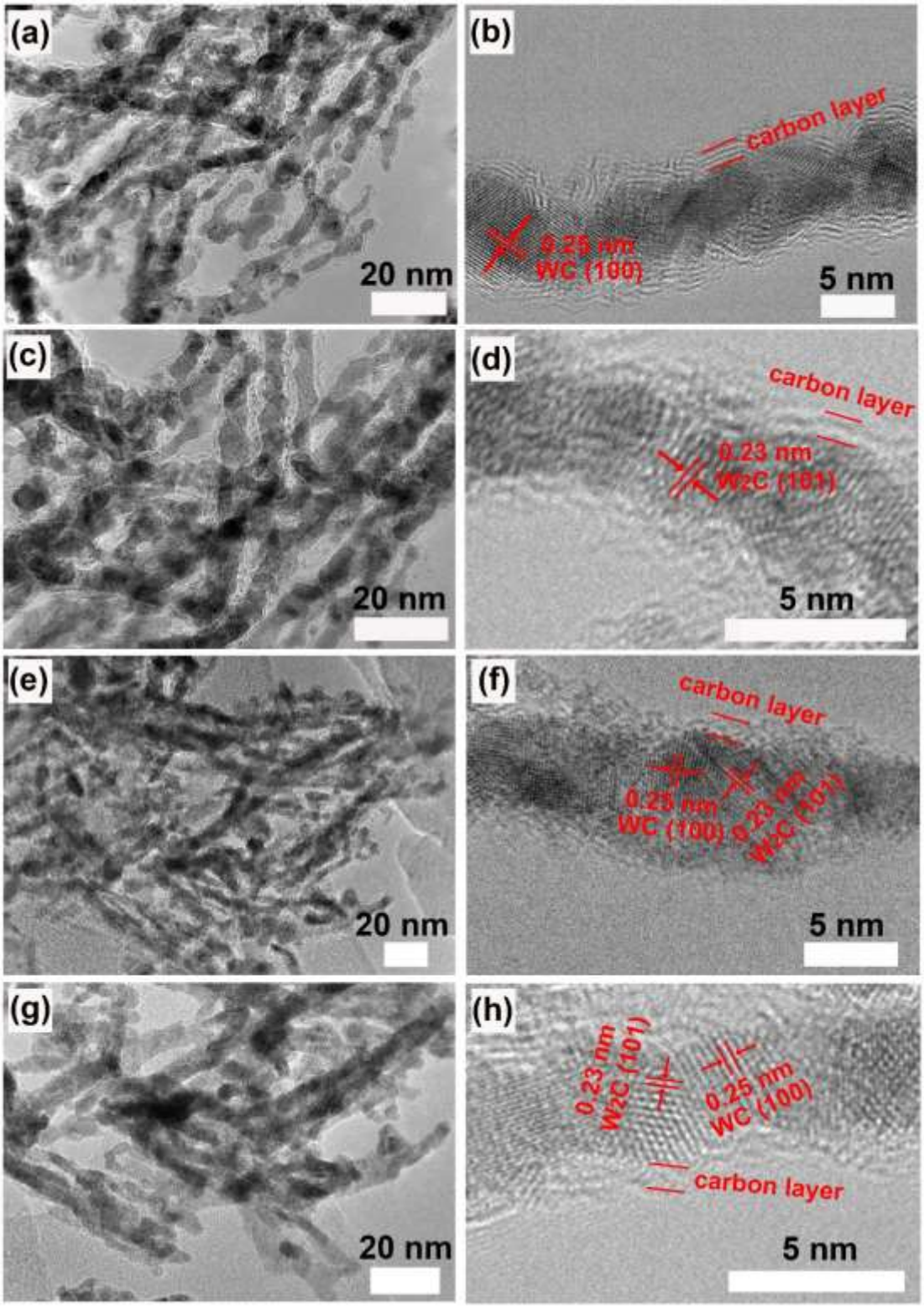

Fig. S4 (a)-(b) TEM images of WC@C NWs; (c)-(d) TEM images of W_2C@C NWs; (e)-(f) TEM images of WC/W_2C@C NWs (WC:W_2C≈1:0.2); (g)-(h) TEM images of WC/W_2C@C NWs (WC:W_2C≈1:6.1).

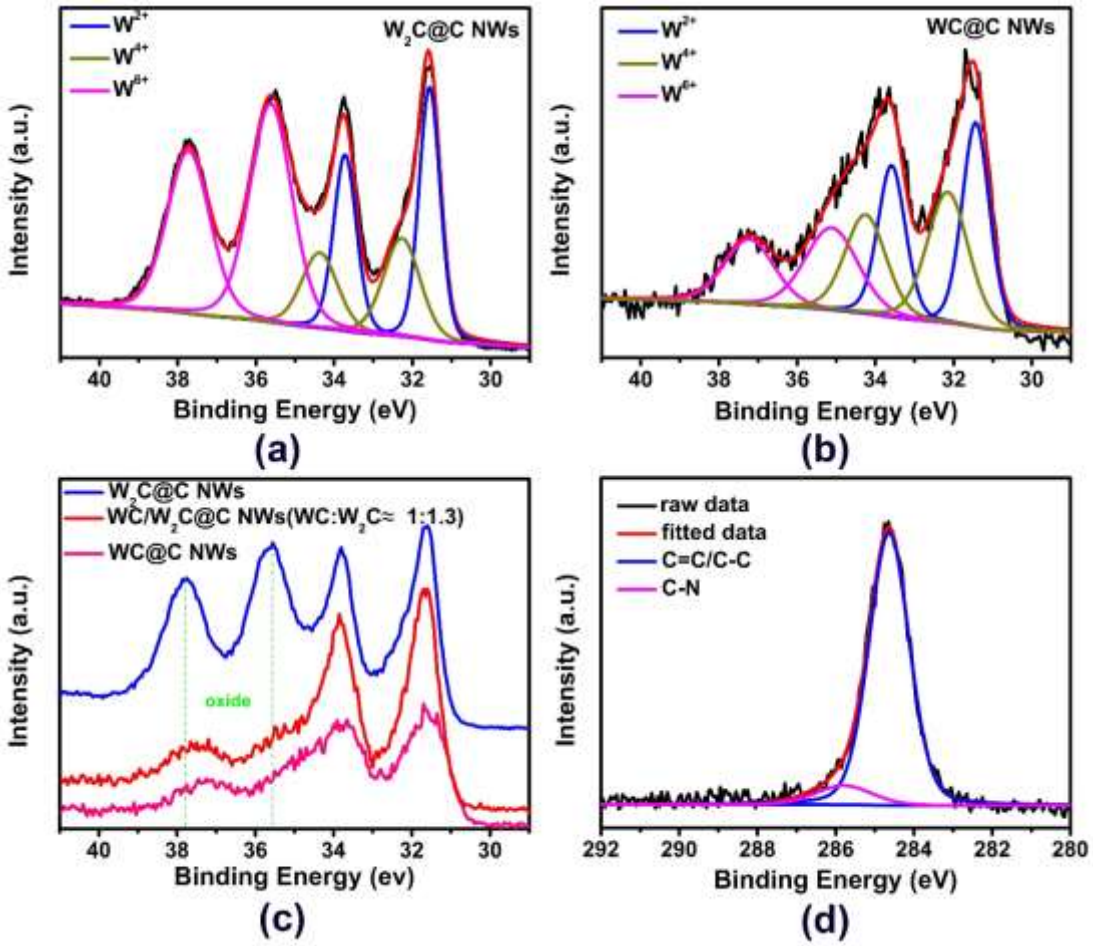

Fig. S5 The high resolution of W 4f XPS spectra of (a) W_2C@C NWs and (b) WC@C NWs; (c) The comparison of high resolution of W 4f XPS spectra of W_2C@C NWs, WC/W_2C@C NWs (WC:W_2C≈1:1.3) and WC@C NWs; (d) The high resolution of C 1s XPS spectrum of WC/W_2C@C NWs (WC:W_2C≈1:1.3).

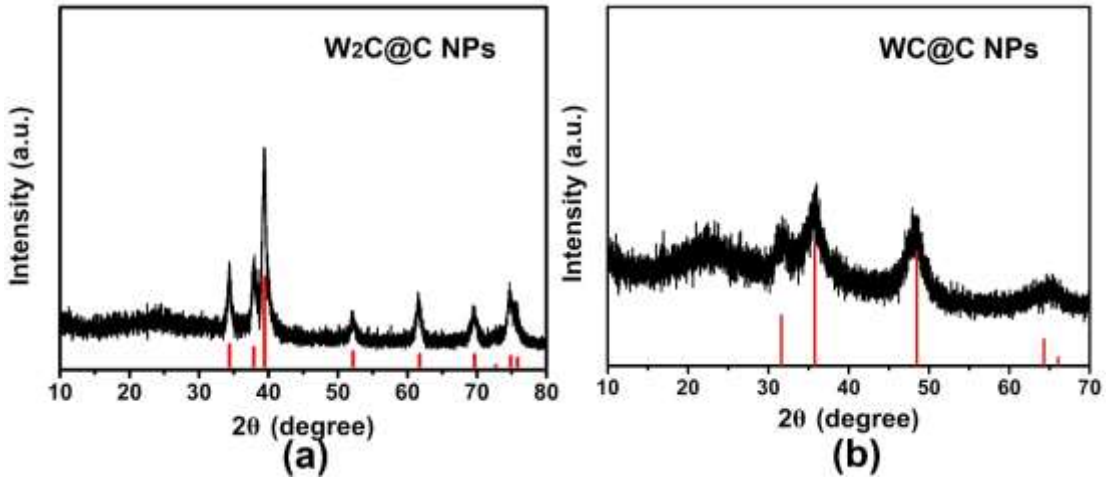

Fig. S6 Powder XRD patterns of (a) W_2C@C NPs and (b) WC@C NPs.

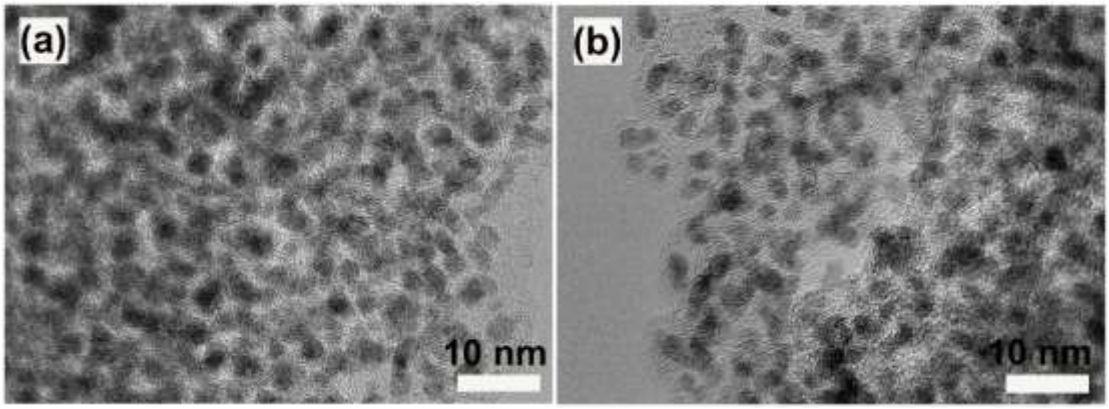

Fig. S7 TEM images of (a) W_2C@C NPs and (b) WC@C NPs. W_2C and WC NPs are both covered with few-layer graphite-like carbon.

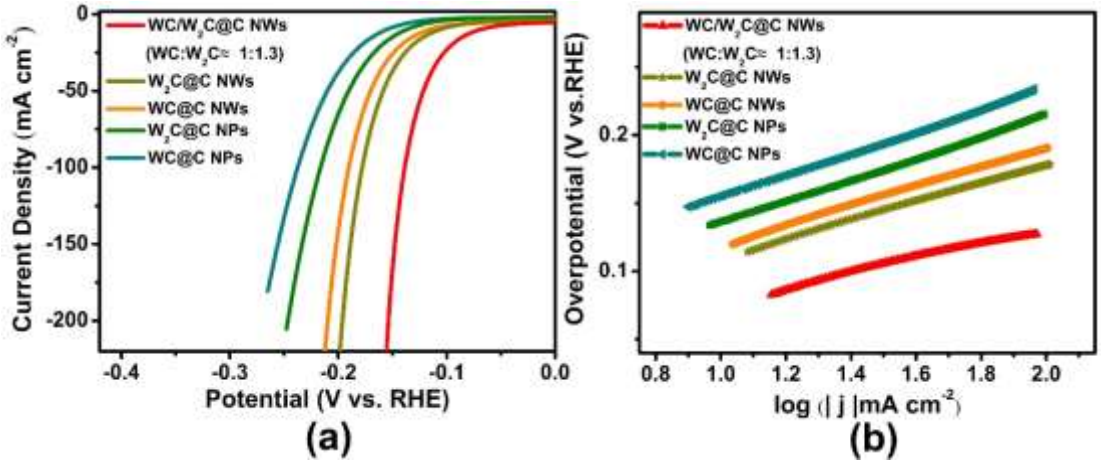

Fig. S8 (a) LSV plots and corresponding Tafel plots of WC/W_2C@C NWs (WC:W_2C≈1:1.3), W_2C@C NWs, WC@C NWs, W_2C@C NPs and WC@C NPs in 0.5 M H_2SO_4.

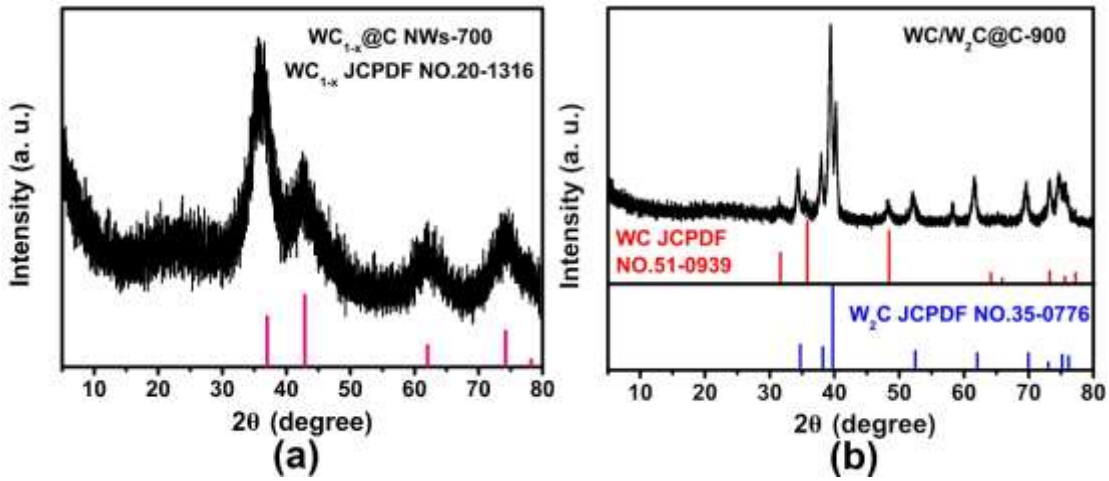

Fig. S9 Powder XRD patterns of (a) WC_{1-x}@C NWs-700 and (b) WC/W_2C@C-900.

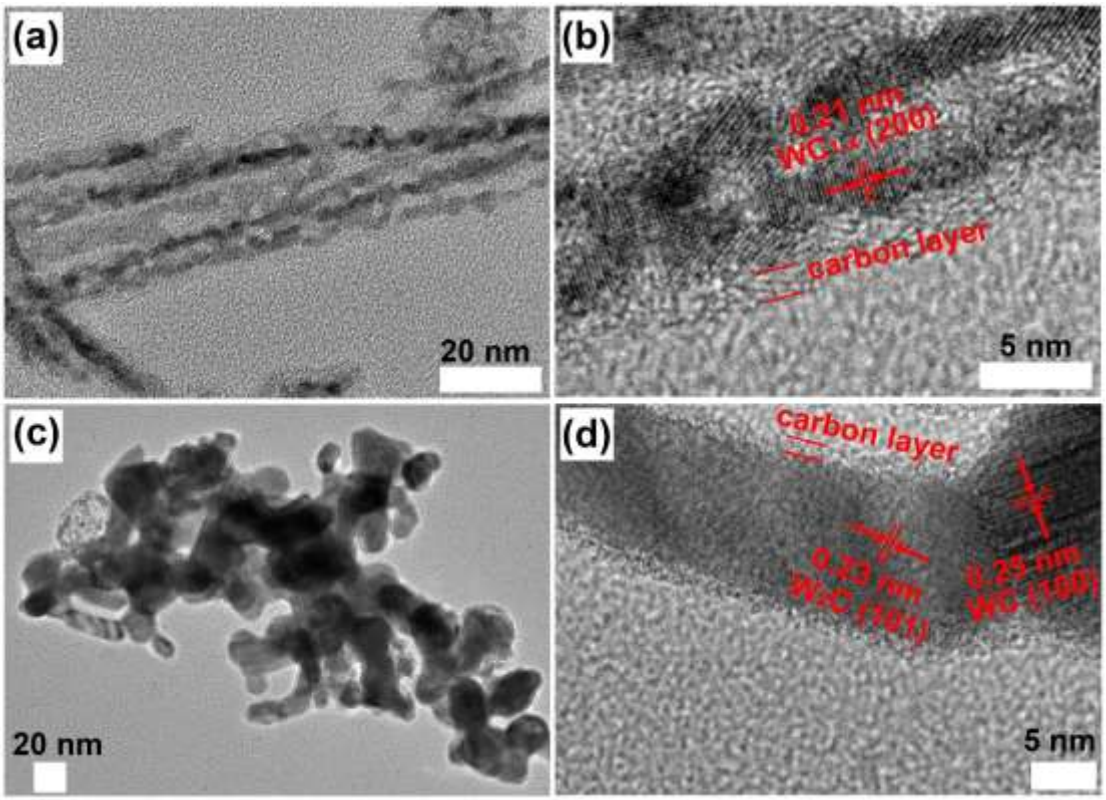

Fig. S10 (a)-(b) TEM images of WC_{1-x}@C NWs-700，tungsten carbides can retain the ultrafine one-dimensional nanowire morphology of $W_{18}O_{49}$ when the carburization temperature is 700 ^{o}C; (c)-(d) TEM images of WC/W_2C@C-900, tungsten carbides failed to retain well the ultrafine one-dimensional nanowire morphology while exists partially sintering when the carburization temperature is 900 ^{o}C.

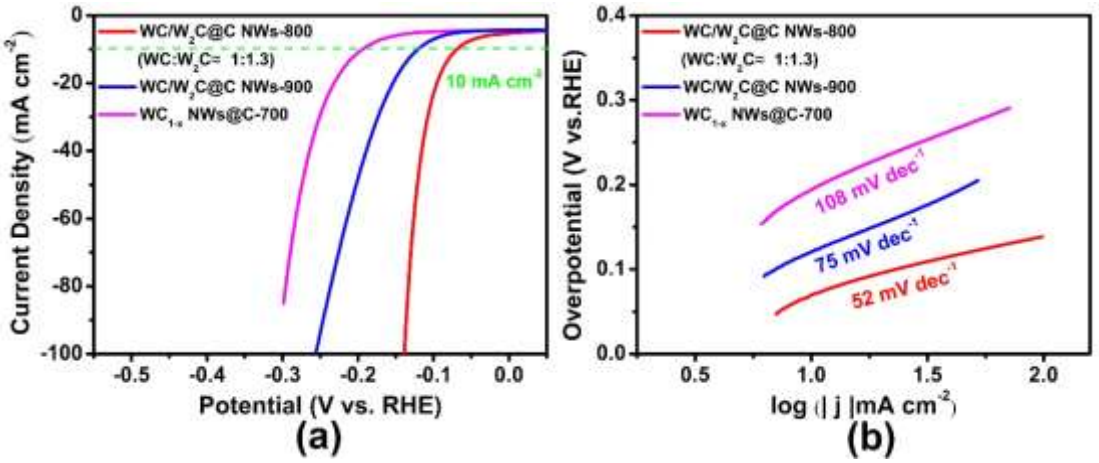

Fig. S11 (a) LSV plots of WC_{1-x}@C NWs-700, WC/W_2C@C NWs-800 (WC:W_2C≈1:1.3) and WC/W_2C@C-900; (b) Tafel curves of WC_{1-x}@C NWs-700, WC/W_2C@C NWs-800 (WC:W_2C≈1:1.3) and WC/W_2C@C-900. The optimal pyrolysis temperature is 800 ^oC, which may be related to the suitable phase composition and well-defined one-dimensional nanowire morphology.

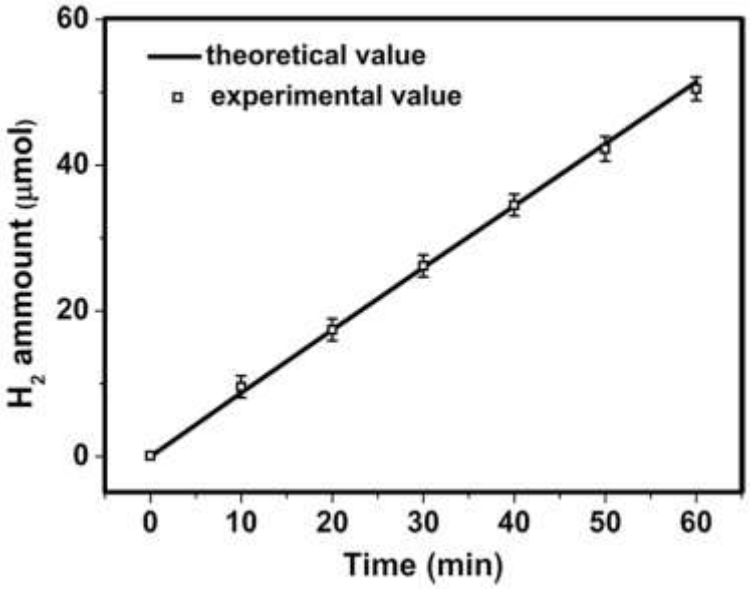

Fig. S12 Faradaic efficiency of WC/W_2C@C NWs (WC:W_2C≈1:1.3) towards HER in 0.5 M H_2SO_4 at the overpotential of 120 mV.

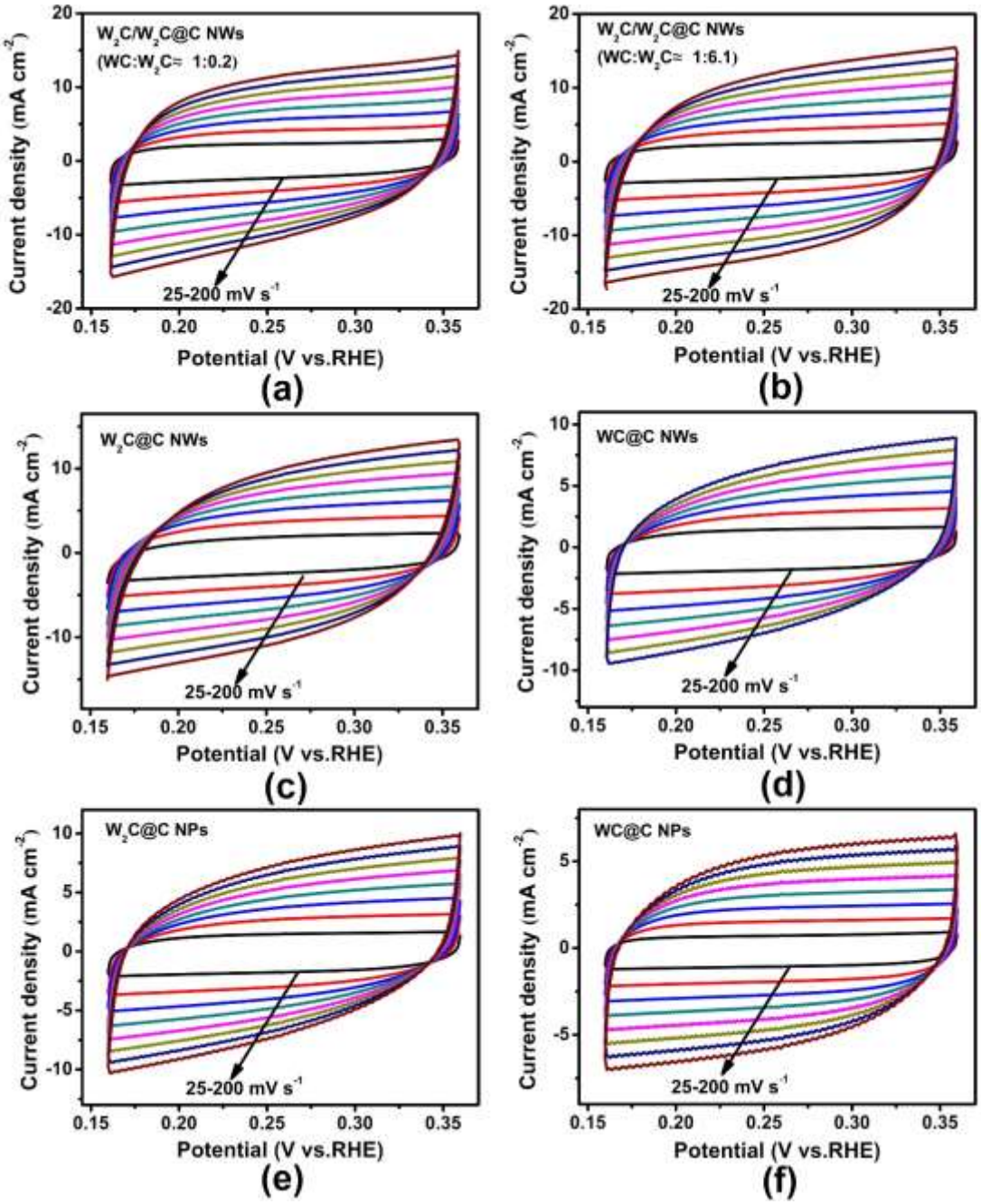

Fig. S13 CV curves of (a) WC/W_2C@C NWs (WC:W_2C≈1:0.2); (b) WC/W_2C@C NWs (WC:W_2C≈1:6.1); (c) W_2C@C NWs; (d) WC@C NWs; (e) W_2C@C NPs and (f) WC@C NPs with different scan rates from 25 to 200 mV s^{-1} in 0.5 M H_2SO_4.

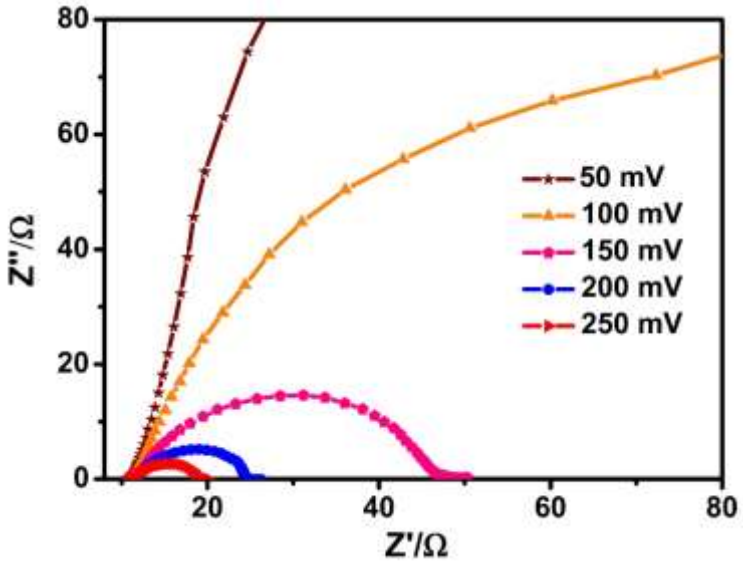

Fig. S14 Electrochemical impedance spectra (EIS) of WC/W_2C@C NWs ($WC:W_2C \approx 1:1.3$) measured with overpotentials from 50 to 250 mV in 0.5 M H_2SO_4.

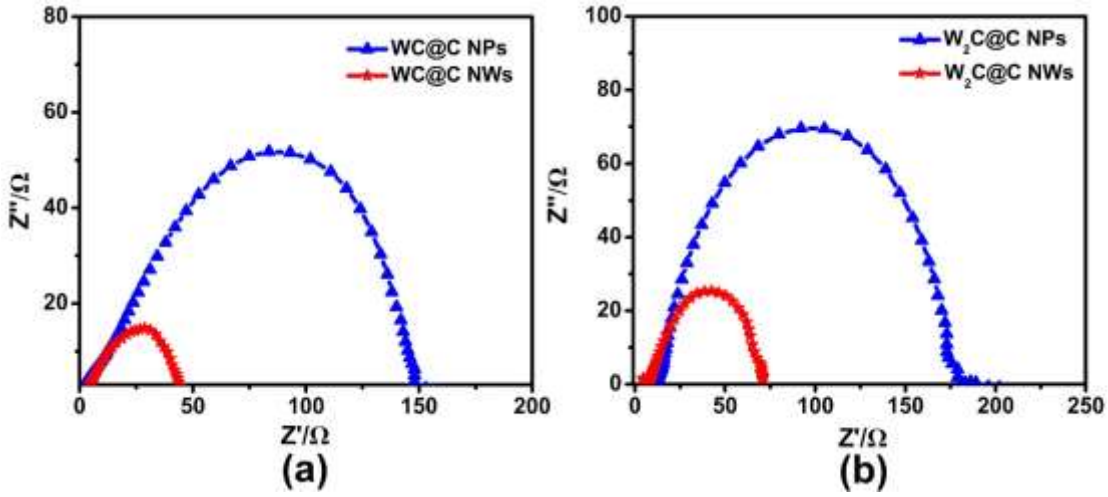

Fig. S15 (a) Nyquist plots of WC@C NWs and WC@C NPs at an overpotential of 150 mV in 0.5 M H_2SO_4; (b) Nyquist plots of W_2C@C NWs and W_2C@C NPs at an overpotential of 150 mV in 0.5 M H_2SO_4.

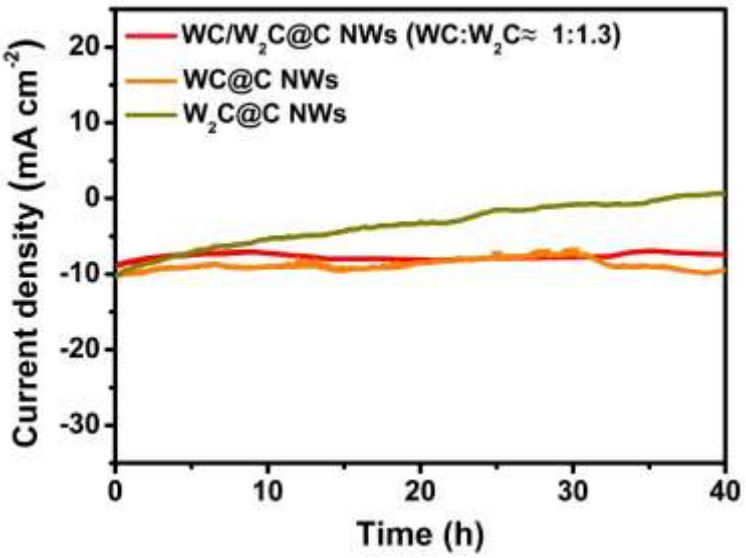

Fig. S16 I-T curves of WC/W_2C@C NWs (WC:W_2C≈1:1.3), WC@C NWs and W_2C@C NWs for 40 h (initial current density = − 10 mA cm^{-2}).

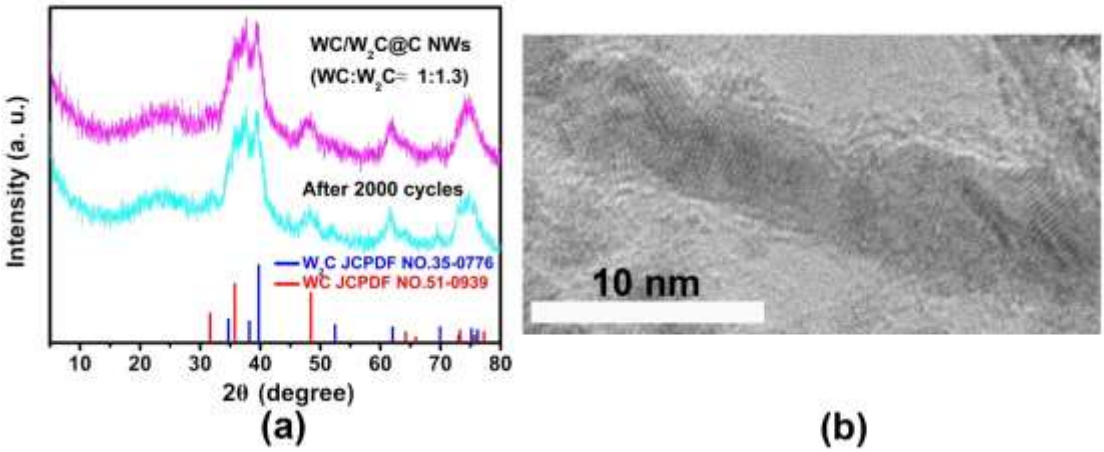

Fig. S17 (a) The PXRD patterns of WC/W_2C@C NWs (WC:W_2C≈1:1.3) (pink line) and after 2000 cycles (blue line). These results reveal that the structure of WC/W_2C@C NWs (WC:W_2C≈1:1.3) can be remained after 2000 cycles HER test; (b) TEM image of WC/W_2C@C NWs (WC:W_2C≈1:1.3) after 2000 cycles test. The image show that the nanowire morphology of WC/W_2C@C NWs (WC:W_2C≈1:1.3) catalyst shows negligible changes.

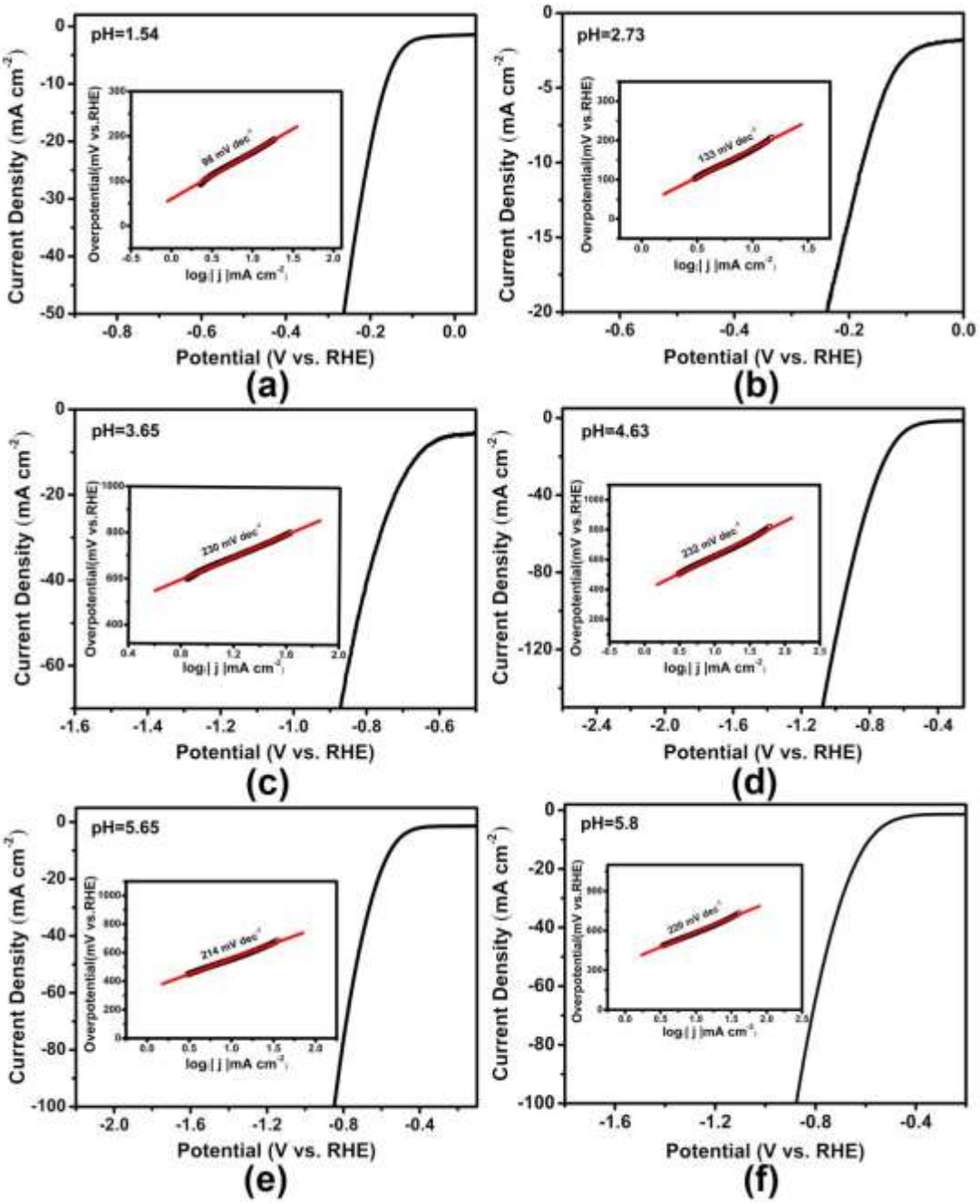

Fig. S18 The HER polarization plots of WC/W_2C@C NWs (WC:W_2C≈1:1.3) in pH (a) 1.54, (b) 2.73, (c) 3.65, (d) 4.63, (e) 5.65 and (f) 5.8 electrolytes at scan rate of 5 mV s^{-1}. Insert: The corresponding Tafel plots of WC/W_2C@C NWs (WC:W_2C≈1:1.3).

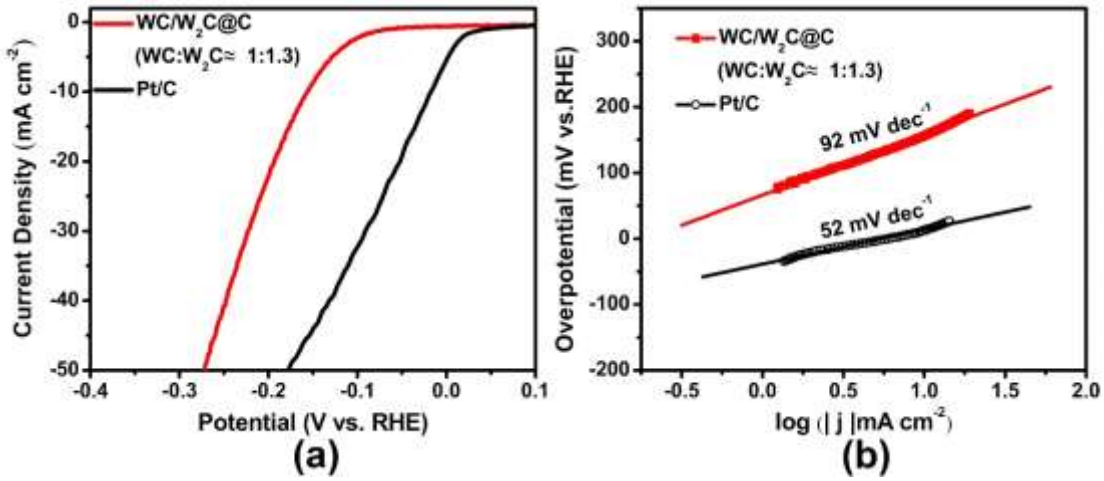

Fig. S19 (a) The HER polarization plots of WC/W_2C@C NWs (WC:W_2C≈1:1.3) and Pt/C in 1 M PBS（pH=7）;(b) The corresponding Tafel plots of WC/W_2C@C NWs (WC:W_2C≈1:1.3) and Pt/C in 1 M PBS.

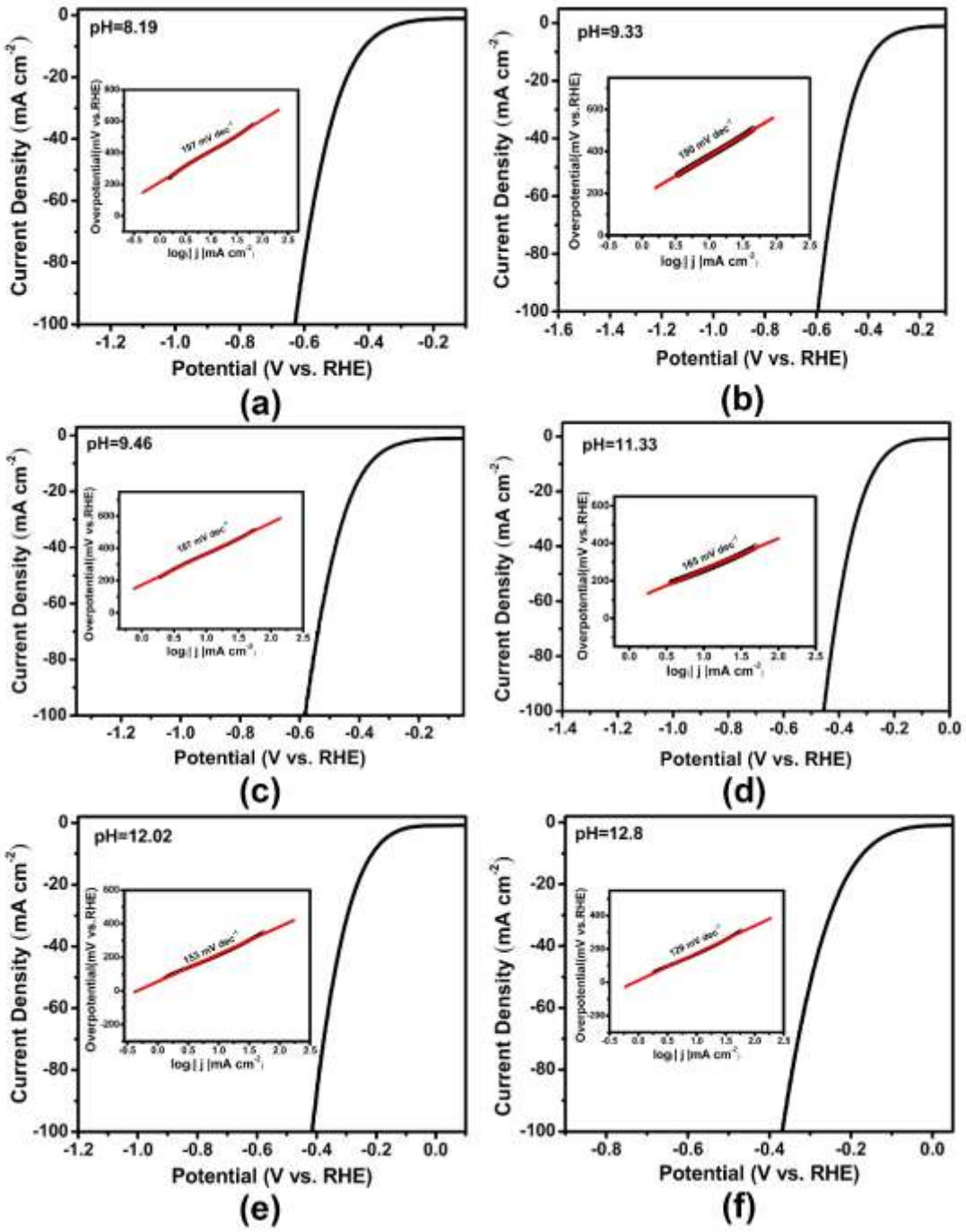

Fig. S20 The HER polarization plots of WC/W_2C@C NWs (WC:W_2C≈1:1.3) in pH (a) 8.19, (b) 9.33, (c) 9.46, (d) 11.33, (e) 12.02 and (f) 12.8 electrolytes at scan rate of 5 mV s^{-1}. Insert: The corresponding Tafel plots of WC/W_2C@C NWs (WC:W_2C≈1:1.3).

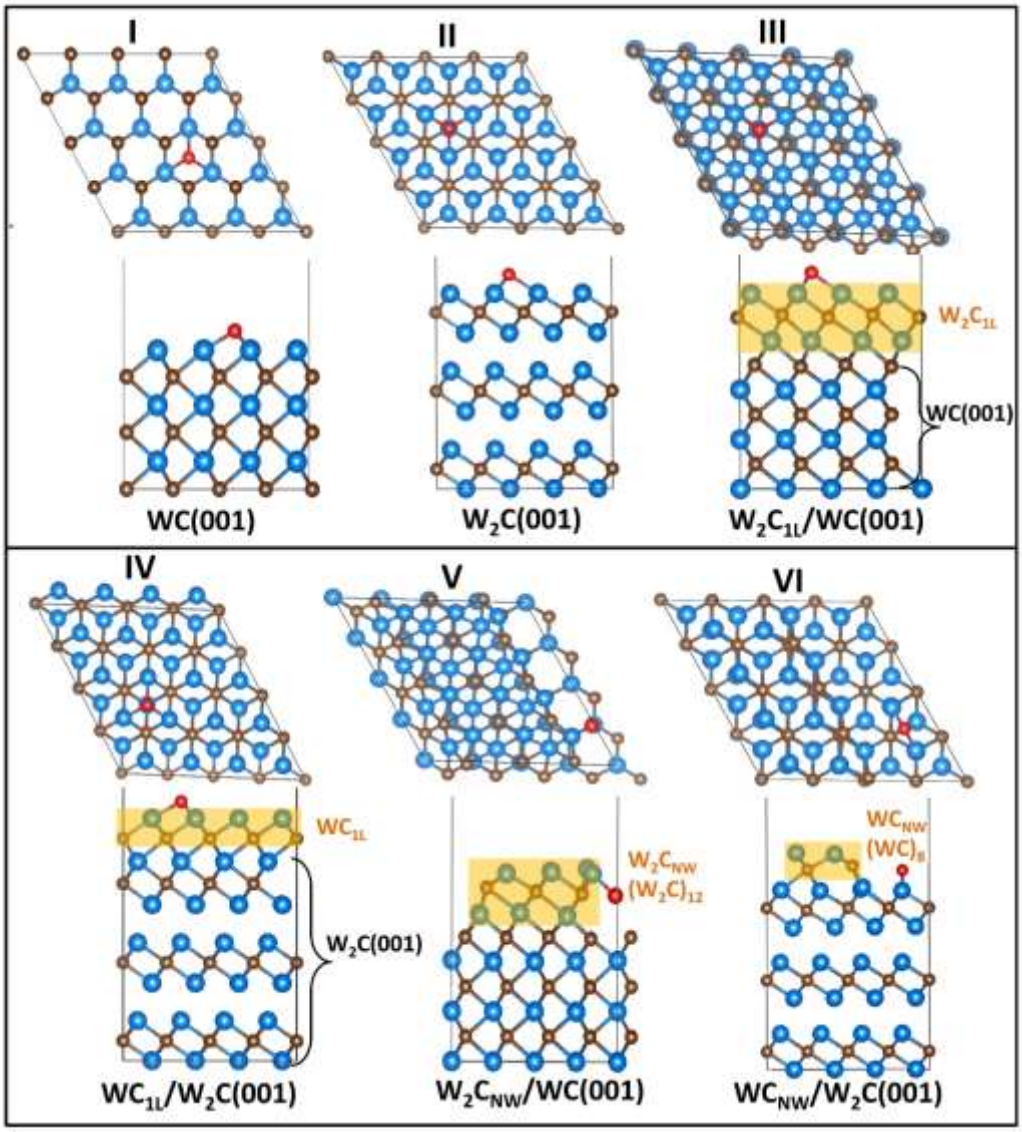

Fig. S21 Theoretical models of the studied systems. Color code: W (light blue), C (brown), and H (red).

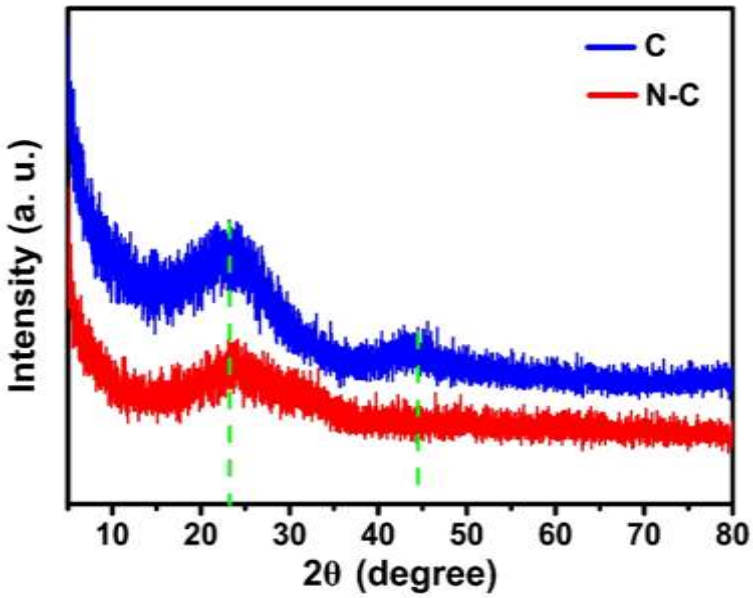

Fig. S22 PXRD patterns of C and N-C. In order to demonstrate the importance of WC in WC/W_2C@C NWs electrocatalysts, N doped carbon (labeled with N-C) and carbon (labeled with C) have been prepared. The preparation method of N-C is as follows: Pure urea was heated to 500 ^oC for 2 h with a heating rate of 2 ^oC min^{-1} in air, the as-obtained C_3N_4 powder was then heated to 800 ^oC for 6 h in N_2 atmosphere with a ramp rate of 5 °C min^{-1}. Carbon without nitrogen (C) is obtained by the pyrolysis of glucose ($C_6H_{12}O_6$) at 800 ^oC for 6 h with a heating rate of 5 °C min^{-1} in N_2. The powder X-ray diffraction (PXRD) patterns of N-C and C show similar characteristic peaks of graphite carbon.

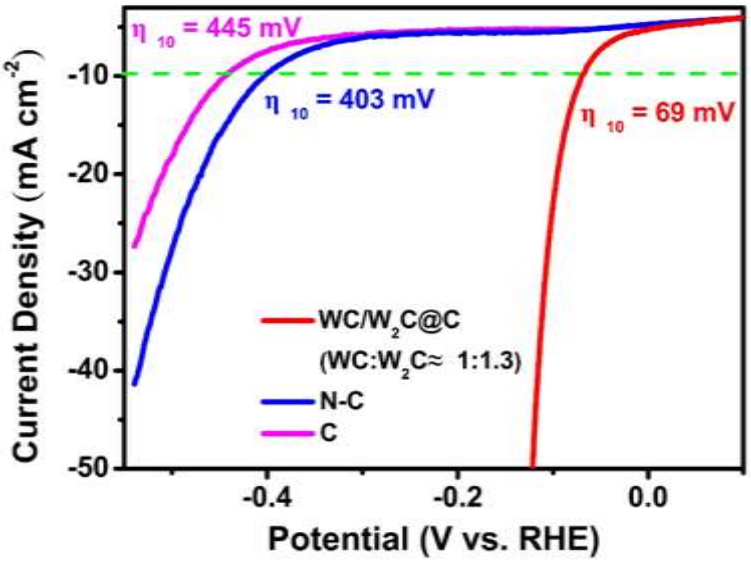

Fig. S23 LSV plots of WC/W_2C@C NWs (WC:W_2C≈1:1.3), N-C and C in 0.5 M H_2SO_4. As shown in Fig. S23, the hydrogen production activity of WC/W_2C@C NWs (WC:W_2C≈1:1.3) is much higher than that of N-C and C, which indicates that tungsten carbide is the real HER electrocatalytic active site in nano-heterojunction catalysts. Furthermore, N-C shows slightly higher HER performance than that of C, confirming the effect of nitrogen doping on improving the HER activities of electrocatalysts.

Supporting Tables

Table S1. Quantitative Analysis from Profile-Fitted PXRD Peaks of WC/W_2C@C NWs.

component / catalyst	WC/%	W_2C/%
WC/W_2C@C NWs ($WC:W_2C \approx 1:0.2$)	84	16
WC/W_2C@C NWs ($WC:W_2C \approx 1:1.3$)	44	56
WC/W_2C@C NWs ($WC:W_2C \approx 1:6.1$)	14	86
The phase composition ratio of WC and W_2C is determined by the PXRD phase quantitative analysis using Jade 6.5		

Table S2. Details for the controlled synthesis of tungsten carbide electrocatalysts from urea and $W_{18}O_{49}$ NWs.

products	the mass ratio of $W_{18}O_{49}$ NWs and urea	temperature (°C)
WC@C NWs	1:200	800
WC/W_2C@C NWs ($WC:W_2C \approx 1:0.2$)	1:150	800
WC/W_2C@C NWs ($WC:W_2C \approx 1:1.3$)	1:100	800

WC/W_2C@C NWs ($WC:W_2C$≈1:6.1)	1:75	800
W_2C@C NWs	1:50	800
WC_{1-x}@C NWs-700	1:100	700
WC/W_2C@C-900	1:100	900

Table S3. The electrochemical parameters of various tungsten-carbide-based electrocatalysts for HER in 0.5 M H_2SO_4.

Cat.	η_{10} (mV)	Tafel slope (mV dec^{-1})	Cdl[a] (mF cm^{-2})	j_0[b] (mA cm^{-2})
WC/W_2C@C NWs ($WC:W_2C$≈1:1.3)	69	52	61	0.361
WC/W_2C@C NWs ($WC:W_2C$≈1:6.1)	80	60	56	0.355
WC/W_2C@C NWs ($WC:W_2C$≈1:0.2)	95	63	49	0.278
W_2C@C NWs	106	68	46	0.241
WC@C NWs	115	71	33	0.211
W_2C@C NPs	137	78	31	0.191
WC@C NPs	155	80	27	0.119

[a]Data are calculated based on the CV results (Figure S12). [b]Exchange current densities (j_0) are obtained from Tafel curves by using extrapolation method.

Table S4. The values of charge transfer resistance (R_{ct}) for W_2C@C NPs, WC@C NPs, W_2C@C NWs, WC@C NWs and WC/W_2C@C NWs ($WC:W_2C$≈1:1.3) at an overpotential of 150 mV in 0.5 M H_2SO_4.

Cat.	R_{ct} (Ω)

W_2C@C NPs	160
WC@C NPs	124
W_2C@C NWs	84.5
WC@C NWs	37.5
WC/W_2C@C NWs (WC:W_2C≈1:1.3)	32.54

Table S5. The values of charge transfer resistance (R_{ct}) and a series resistance (R_s) for WC/W_2C@C NWs (WC:W_2C≈1:1.3) with overpotential from 50 to 250 mV in 0.5 M H_2SO_4.

Potential (mV *vs.* RHE)	WC/W_2C@C NWs (WC:W_2C≈1:1.3)	
	R_{ct} (Ω)	R_s (Ω)
50	1524	11.20
100	168	11.28
150	32.54	11.26
200	11.84	11.07
250	6.53	11.10

Table S6. Comparison of catalytic parameters of WC/W_2C@C NWs ($WC:W_2C \approx 1:1.3$) in different electrolytes.

pH value	Overpotential at 10 mA cm^{-2} (mV vs RHE)	Tafel slope (mV dec^{-1})
0.3	69	52
1.54	162	98
2.73	176	133
3.65	649	230
4.63	621	232
5.65	552	214
5.8	583	220
7.0	155	92
8.19	412	197
9.33	378	190
9.46	365	187
11.33	256	165
12.02	212	153
12.8	169	129
14.0	56	59

Table S7. Comparison of HER performance in acidic and alkaline media for WC/W_2C@C NWs (WC:W_2C≈1:1.3) with other W-based HER elecrocatalysts.

Catalyst	Overpotential (mV) in 0.5 M H_2SO_4	Overpotential (mV) in 1 M KOH	Ref.
WC/W_2C@C NWs (WC:W_2C≈1:1.3)	**69**	**56**	**This work**
WC-CNTs	145	137	[S8]
$(Mo_2C)_{0.34}$–$(WC)_{0.32}$/NG	100	93	[S9]
W_2C@GL	135	N.A.	[S10]
p-WC_x NWs	118	122	[S11]
WOx/C NWs	108	N.A.	[S12]
C-CWC	200	73	[S13]
Ni-S-W-C	N.A.	262 (in 30% KOH solution)	[S14]
WSe_2 nanofilms	189	N.A.	[S15]
C-WP/W	109	133	[S16]
W_xC/NG-10	77.82	N.A.	[S17]
W/BrN	148	94	[S18]
CoS_2@WS_2	97.2	N.A.	[S19]
Mo-W-S/CC	198	N.A.	[S20]

$W_{18}O_{49}$ NFs	425	N.A.	[S21]
WP_2 SMPs	161	153	[S22]
W_2C-NC-WN	N.A.	145	[S23]
i-WC–G	120	225 (0.1 M KOH)	[S24]
PWC	274	N.A.	[S25]
Co_2P/WC@NC	91	180	[S26]

The detailed HER mechanism in heterojunction catalysts

In principle, the HER pathway in acidic solution can be depicted as three steps: the adsorption of H^+ on the surface of catalyst, the reduction of H^+ to adsorbed H (H_{ads}) on catalyst, and the desorption of H_{ads} to generate H_2. Regarding the overall HER process, a good hydrogen catalyst should have a free energy (ΔG_H*) for H adsorption close to zero and a suitable bond strength between the surface of catalyst and H_{ads}, which is favourable for the adsorption of proton and the desorption of H_2. According to the results of our DFT calculations, charge rearrangement occurs at the two phase interfaces in one-dimensional WC/W_2C heterojunction nanowires, which endows the catalysts with optimized electronic configuration and suitable ΔG_H*. The intrinsic hydrogen production activities of two components have been synergistically improved, which is similar to other heterojunction HER catalysts (eg. Fe_3C-Mo_2C hetero-nanofibers,[S27] MoC-Mo_2C heteronanowires[S28]). Besides the above, the conductivity and stability of our WC/W_2C heterojunction catalysts have also been obviously enhanced by constructing multiple two-phase heterojunction interfaces. That is to say, in WC/W_2C heterojunction nanowires, the decent HER performance is not only due to the improvement of intrinsic hydrogen production activity of two components, but also attributed to the enhancement on its conductivity and stability.

References

[S1] G. Kresse, J. Hafner, *Phys. Rev. B: Condens. Matter Mater. Phys.*, 1993, **47**, 558.

[S2] G. Kresse, J. Hafner, *Phys. Rev. B: Condens. Matter Mater. Phys.*, 1994, **49**, 14251.

[S3] G. Kresse, J. Furthmuller, *Comput. Mater. Sci.*, 1996, **6**, 15.

[S4] G. Kresse, J. Furthmuller, *Phys. Rev. B: Condens. Matter Mater. Phys.*, 1996, **54**, 11169.

[S5] P. E. Blöchl, *Phys. Rev. B.*, 1994, **50**, 17953.

[S6] J. Hafner, *J. Comput. Chem.*, 2008, **29**, 2044.

[S7] H. J. Monkhorst, J. D. Pack, *Phys. Rev. B: Solid State.*, 1976, **13**, 5188.

[S8] X. Fan, H. Zhou, X. Guo, *ACS. Nano.*, 2015, **9**, 5125.

[S9] L. Huo, B. Liu, Z. Gao, J. Zhang, *J. Mater. Chem. A*, 2017, **5**, 18494.

[S10] Y. Zhou, R. Ma, P. Li, Y. Chen, Q. Liu, G. Cao, J. Wang, *J. Mater. Chem. A*, 2016, **4**, 8204.

[S11] B. Ren, D. Li, Q. Jin, H. Cui, C. Wang, *J. Mater. Chem. A*, 2017, **5**, 13196.

[S12] C. Liu, Y. Qiu, Y. Xia, F. Wang, X. Liu, X. Sun, Q. Liang, Z. Chen, *Nanotechnology*, 2017, **28**, 445403.

[S13] Y. Liu, G. Li, L. Yuan, L. Ge, H. Ding, D. Wang, X. Zou, *Nanoscale*, 2015, **7**, 3130.

[S14] Y. Wu, H. He, *Materials Letters*, 2017, **209**, 532.

[S15] H. Li, J. Zou, S. Xie, X. Leng, D. Gao, H. Yang, X. Mao, *Journal of Alloys and Compounds*, 2017, **725**, 884.

[S16] L. Wu, Z. Pu, Z. Tu, I. S. Amiinu, S. Liu, P. Wang, S. Mu, *Chemical Engineering Journal*, 2017, **327**, 705.

[S17] J. Wang, W. Chen, X. Wang, E. Wang, *Electrochimica Acta*, 2017, **251**, 660.

[S18] Q. Li, C. Han, X. Ma, D. Wang, Z. Xing, X. Yang, *J. Mater. Chem. A*, 2017, **5**, 17856.

[S19] X. Zhou, X. Yang, H. Li, M. N. Hedhili, K. W. Huang, L. Li, W. Zhang, *J. Mater. Chem. A*, 2017, **5**, 15552.

[S20] C. Li, X. Bo, M. Li, L. Guo, *Int J Hydrogen Energ*, 2017, **42**, 15479.

[S21] Y. Zhao, Q. Tang, B. He, P. Yang, *Int J Hydrogen Energ*, 2017, **42**, 14534.

[S22] Z. Xing, Q. Liu, A. M. Asiri, X. Sun, *ACS Catal.*, 2015, **5**, 145.

[S23] S. C. Abbas, J. Wu, Y. Huang, D. D. Babu, G. Anandhababu, M. A. Ghausi, M. Wu, Y. Wang, *Int J Hydrogen Energ*, 2018, **43**, 16.

[S24] M. Zeng, Y. Chen, J. Li, H. Xue, R. G. Mendes, J. Liu, T. Zhang, M. H. Rümmeli, L. Fu, *Nano Energy*, 2017, **33**, 356.

[S25] H. Fei, Y. Yang, X. Fan, G. Wang, G. Ruan, J. M. Tour, *J. Mater. Chem. A*, 2015, **3**, 5798.

[S26] Y. Gao, Z. Lang, F. Yu, H. Tan, G. Yan, Y. Wang, Y. Ma, Y. Li, *ChemSusChem*, 2018, **11**, 1082.

[S27] H. Lin, W. Zhang, Z. Shi, M. Che, X. Yu, Y. Tang, Q. Gao, *ChemSusChem*, 2017, **10**, 2597.

[S28] H. Lin, Z. Shi, S. He, X. Yu, S. Wang, Q. Gao, Y. Tang, *Chem. Sci.*, 2016, **7**, 3399.